Article

Spectroscopic and Spectroelectrochemical Studies on Redox Properties of Zinc Sulfide and Their Consequences on Photocatalytic Activity

Krystian Mróz, Marcin Kobielusz,* Łukasz Orzeł, and Wojciech Macyk*

Read Online

ACCESS | 📊 Metrics & More | 📖 Article Recommendations | 🆂�🅸 Supporting Information

ABSTRACT: Understanding the relationships between the electronic structure (and therefore redox properties) of semiconductors and their photoactivity is crucial for a rational design of photocatalysts. In this work, we undertake such analysis with the help of emission and absorption UV–vis spectroscopy, as well as diffuse reflectance spectroelectrochemistry (SE-DRS). Herein, we focus on zinc sulfide, which is considered a photocatalyst with strong reducing properties but is also known for its efficient visible light photoluminescence. A series of ZnS materials with a different Zn:S ratio was synthesized, in an anaerobic and oxygen atmosphere. The synthesized samples were thoroughly studied in terms of morphological, photophysical, and photocatalytic properties. Two groups of materials (sulfur-rich and sulfur-deficient) could be distinguished, with significantly different properties, such as the crystal size, oxygen concentration, bandgap energy, distribution of electronic states, and photoelectrocatalytic and photocatalytic activities. We confirmed the presence of deep electronic states, which significantly decrease the reduction abilities of ZnS, some of which are surface states. Models of the electronic structures associated with possible photophysical processes were proposed for both sulfur-rich and sulfur-deficient materials. Although in proposed models the energy of photogenerated electrons is significantly lower than that usually considered based on the level of the conduction band edge, the photocatalytic tests revealed their sufficient potential to perform hydrogen evolution and CO_2 reduction processes.
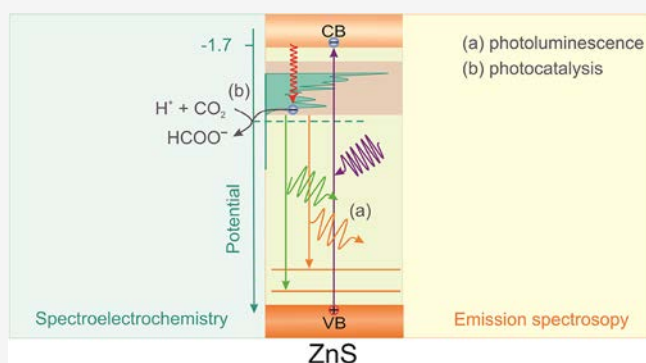
INTRODUCTION

Zinc sulfide is a widely known semiconductor, which exists mainly in the forms of hexagonal wurtzite and cubic sphalerite.[1] ZnS is an inexpensive and easy-to-prepare material that offers good charge carrier mobility and reasonable photostability.[2,3] It has a wide bandgap (from 3.3 to 3.8 eV),[4–8] which narrows its activity to the UV-light range. ZnS nanomaterials have been recently tested in the processes of photocatalytic organic pollutant degradation,[9–11] CO_2 reduction,[12–14] water splitting,[15,16] and photocatalytic organic syntheses.[17–20] Due to the very negative potential of its conduction band edge, it appears a particularly promising photocatalyst in energy-demanding processes like CO_2 and water reduction.[1,21] Zinc sulfide is also well-known for its light emission properties, which are usually related to the presence of interband states.[22–24] The emission spectrum is usually composed of green (513–530 nm) and blue (435–450 nm) emissions. The observed significant red shift of the emission points to a considerable energy difference between the interband states and the band edge. These states originate mostly from surface and bulk defects (vacancies, dopant atoms, etc.) in the ZnS structure. Like other sulfides, also in the case

of ZnS, oxygen can induce both types of defects.[19,22,25–27] The presence of electronic states characterized by lower energy values compared to the CB edge may decrease significantly the semiconductor reduction abilities. Therefore, understanding the electronic structure of such materials is crucial to predicting their photocatalytic properties.

The energy model of the semiconductor can be constructed based on the analysis of emission and absorption spectra. However, this approach is blind to these states that are not involved in radiative emission processes. Applying a method such as reverse double-beam photoacoustic spectroscopy (RDB-PAS) gives the possibility of mapping the distribution of electron traps within the band gap and conduction band independently of their involvement in emission processes.[22,28,29] However, both PL and RDB-PAS make it

possible to locate these states only *versus* the conduction band, the potential of which varies in the literature. To determine the redox properties of zinc sulfide ultimately, it is necessary to describe the electronic structure using a univocal energy scale. A recently modified spectroelectrochemical method may potentially be a good solution to address this problem.[26,27] The combination of electrochemical reduction with diffuse reflectance spectroscopy (SE-DRS) allows us to describe the distribution of electronic states quasi-quantitatively at the potential scale.

To the best of the authors' knowledge, so far no attempt was undertaken to combine spectroelectrochemical and spectroscopic approaches for a comprehensive analysis of the electronic structure of semiconductors, in particular zinc sulfide. Understanding the influence of various parameters, like conditions of synthesis, on the electronic structure of ZnS may facilitate the rational optimization of this material toward photocatalytic applications. Our goal is to characterize the electronic structure of ZnS and determine how the application of different Zn:S ratios may influence it and, therefore, how it affects the photocatalytic activity of ZnS, especially in the applications to CO_2 and water reduction processes.

■ EXPERIMENTAL SECTION

Materials and Reagents. The chemicals used in the experiments (AgNO$_3$, TBAP, LiClO$_4$, CH$_3$CN, BaSO$_4$, NaHCO$_3$, thiourea, NaOH, 2,5-dihydrofuran, and ZnSO$_4$) were supplied by Sigma-Aldrich. Photoelectrochemical measurements were carried out in 0.1 mol dm^{-3} Na$_2$SO$_4$ in water as an electrolyte.

Synthesis of ZnS Photocatalysts. ZnS materials were prepared as previously reported by Hörner et al.[30] A solution of NaOH (20.0 g, 0.5 mol) and ZnSO$_4$·7H$_2$O (5.75 g, 0.02 mol) in H$_2$O (100 mL) was prepared. After the redissolution of Zn(OH)$_2$, with the formation of [Zn(OH)$_4$]$^{2-}$, the solution of thiourea was added to the final volume of 160 mL. The mixture was heated to 80 °C for 48 h, under an argon atmosphere. The powder was washed with H$_2$O to neutrality and dried at 60 °C. Materials were synthesized with different Zn:S ratios (ZnS(1:0.66), ZnS(1:1), ZnS(1:1.33), and ZnS(1:1.5)). The synthesis of ZnS(1:1) was performed additionally under the oxygen atmosphere (ZnS(1:1)-O$_2$) and with the use of oxygen plasma treatment (12 min, 0.4 bar, Diener Electronic Plasma Surface Generator Zepto, material labeled as ZnS(1:1)-plasma).

Material Characterization. The X-ray diffraction patterns were recorded using a Rigaku MiniFlex 600. The nanocrystalline powders were pressed inside the sample holder, and the X-ray diffraction data were collected in a step scan mode. The X-ray radiation source was Cu K$_\alpha$, operating at 40 kV, 15 mA. The scanning rate was 1°/min at a step of 0.05°.

Morphology and agglomeration of materials were analyzed with scanning electron microscopy (SEM; VEGA 3, Tescan), after sputtering with gold (Quorum Q150T).

Elemental analysis of sulfur content was performed using the Vario Micro Cube analyzer (Elementar). The zinc content was analyzed using the PinAAcle 900F flame atomic absorption spectroscope (FAAS) (PerkinElmer). For effective mineralization, concentrated nitric acid and the ERTEC Magnum microwave mineralizator were utilized.

A Thermo Scientific K-Alpha X-ray Photoelectron Spectrometer (XPS) equipped with an aluminum anode (Al K$_\alpha$ = 1468.3 eV) was used to unravel the elemental composition of the studied materials. The electron take-off angle between the film surface and the axis of the analyzer lens was set to 90°. The flood gun was used to reduce surface charging. Advantage 5.9 software was used to record and manipulate the spectra. Moreover, the C 1s peaks at the binding energy of 284.5 eV were used as a reference to correct the energy shift caused by charging.

Photophysical Characterization. Diffuse reflectance spectra of obtained materials were measured using a UV−vis spectrophotometer (Shimadzu UV-3600) equipped with an integrating sphere. Samples were mixed with BaSO$_4$, and then diffuse reflectance spectra of formed pellets were recorded. Bare barium sulfate was used as a reference material.

Photoluminescence studies were carried out using a Fluorolog-3 (Horiba Jobin Yvon) spectrofluorimeter equipped with a solid-state sample holder and a dual excitation source. The 450 W xenon lamp was used in the measurements of the emission spectra. 2D maps were collected using cutoff filters (450 and 500 nm separately to the particular excitation wavelength sections) to exclude excitation components from spectra. The emission spectra were deconvoluted with the use of the multiple-peak fit option included in the OriginPro 2021b software. The 2D spectra were corrected using the internal correction function.

Lifetimes of the excited states were determined using a series of NanoLEDs with picosecond-range pulse width as the excitation source. The kinetic traces of emission decay were fitted with an exponential function.

Spectroelectrochemical Measurements. Working electrodes were prepared by casting examined materials, previously ground in a mortar with a few drops of acetonitrile, at the surface of the platinum plate (*ca.* 1.5 × 4 cm^2). The electrodes were dried at approximately 60 °C, resulting in the formation of opaque films. The measurements were carried out in a three-electrode cell (quartz cuvette), with platinum wire and Ag/Ag$^+$ (10 mmol dm^{-3} AgNO$_3$ in acetonitrile solution of 0.1 mol dm^{-3} TBAP) as the counter and reference electrodes, respectively. 0.1 mol dm^{-3} LiClO$_4$ in acetonitrile was used as the electrolyte. The quartz cuvette was placed in front of the sphere, facing the working electrode (platinum plate with a deposited semiconductor) toward the light beam. The potential control was provided by the electrochemical analyzer BioLogic SP-150 with a step scan mode (0.05 V per 20 min). Relative reflectance changes, recorded versus the reflectance measured for the same system directly before the measurement, were collected by a Shimadzu 3600 UV−Vis−NIR spectrometer equipped with the integrating sphere. The reflectance was recorded at an 800 nm wavelength.
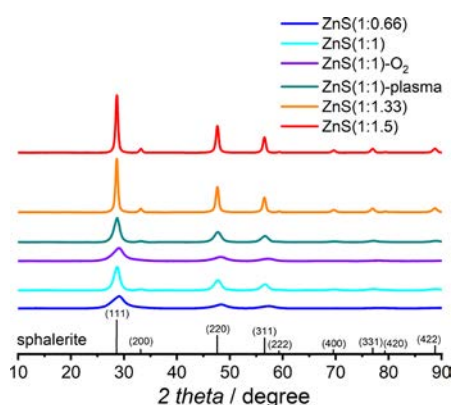
■ PHOTOACTIVITY

Photoelectrochemical measurements were carried out in a three-electrode setup. The electrolyte (0.1 mol dm^{-3} Na$_2$SO$_4$) was purged with argon for at least 5 min before and during the measurements. A platinum wire and Ag/AgCl were used as the counter and reference electrodes, respectively. A photoelectrochemical spectrometer (Instytut Fotonowy), equipped with a 150 W xenon lamp (XBO 150) with a water-cooled housing and an automatically controlled monochromator, was used. The working electrodes (ITO coated with a transparent foil of 60 Ω/sq. resistance, Sigma-Aldrich, with the casted and dried material) were irradiated from the backside through the ITO layer.

The photocatalytic efficiency of studied materials was determined by measuring the concentration of evolved hydrogen. 10 mg of the photocatalyst was suspended in 9.5 mL of water, and then 0.5 mL of 2,5-dihydrofuran was added. The mixture was placed in an optical glass cuvette (5 cm diameter, 1 cm optical path, and 15 mL volume) equipped with a magnetic stirrer. The suspension was irradiated with a 150 W xenon lamp (XBO 150, Instytut Fotonowy) through an NIR filter (10 cm, 0.1 mol dm^{-3} CuSO$_4$ solution in water) and a 320 nm cutoff filter. The samples were collected after 0, 45, 90, 135, and 180 min. The concentration of photogenerated H$_2$ was determined with the use of GC (Thermo Scientific TRACE 1300 Gas Chromatograph equipped with TCD, FID detectors, and Carboxen 1010 PLOT Capillary Column). A similar setup was used in CO$_2$ reduction tests. In the cuvette, 10 mg of the photocatalyst was suspended in 10 cm^3 of water and then NaHCO$_3$ was added until the final concentration of 0.1 mol dm^{-3} was reached. The samples were collected after 0, 90, 180, 270, and 360 min of irradiation. The concentration of photogenerated HCOOH was determined in the aqueous phase with the use of HPLC (Shimadzu Prominence-i LC-2030 3D Liquid Chromatograph equipped with a Diode Array UV−vis detector and an Agilent ZORBAX SB-Aq analytical 4.6 × 150 mm column).

■ RESULTS AND DISCUSSION

Material Characterization. Six powder materials have been synthesized by the method proposed by Kisch et al.[30] Precipitation of ZnS was achieved by mixing ZnSO$_4$ solution with thiourea under an oxygen-free atmosphere with various Zn^{2+}:thiourea molar ratios. The resulting materials are labeled as ZnS(1:x), where 1:x is the molar ratio of the substrates. Zn(1:0.66) and ZnS(1:1) are white powders, while ZnS(1:1.33) and ZnS(1:1.5) are peach-colored. Furthermore, to investigate oxygen's influence on material properties, ZnS(1:1) was additionally treated with oxygen plasma (labeled as ZnS(1:1)−plasma) and the synthesis of ZnS(1:1) was repeated in an oxygen-rich atmosphere, yielding ZnS(1:1)−O$_2$. In this way, the possible surface and mixed surface/bulk oxygen defects were introduced to the ZnS sample. The material structures and particle sizes were determined by powder X-ray diffraction (XRD) measurements (Figure 1). All materials were crystallized in a sphalerite form; however, they differ in crystal sizes (Table S1). ZnS(1:1.33) and ZnS(1:1.5) are characterized by larger particle sizes (18−21 nm, calculated

based on Debye−Scherrer and Williamson−Hall approximations) compared to ZnS(1:0.66) and ZnS(1:1) samples (3 and 7−8 nm, respectively). It can be observed that the material synthesized under the oxygen atmosphere (ZnS(1:1)−O$_2$) is composed of smaller particles compared to ZnS(1:1). However, the surface plasma treatment does not change the material structure and its particle size.
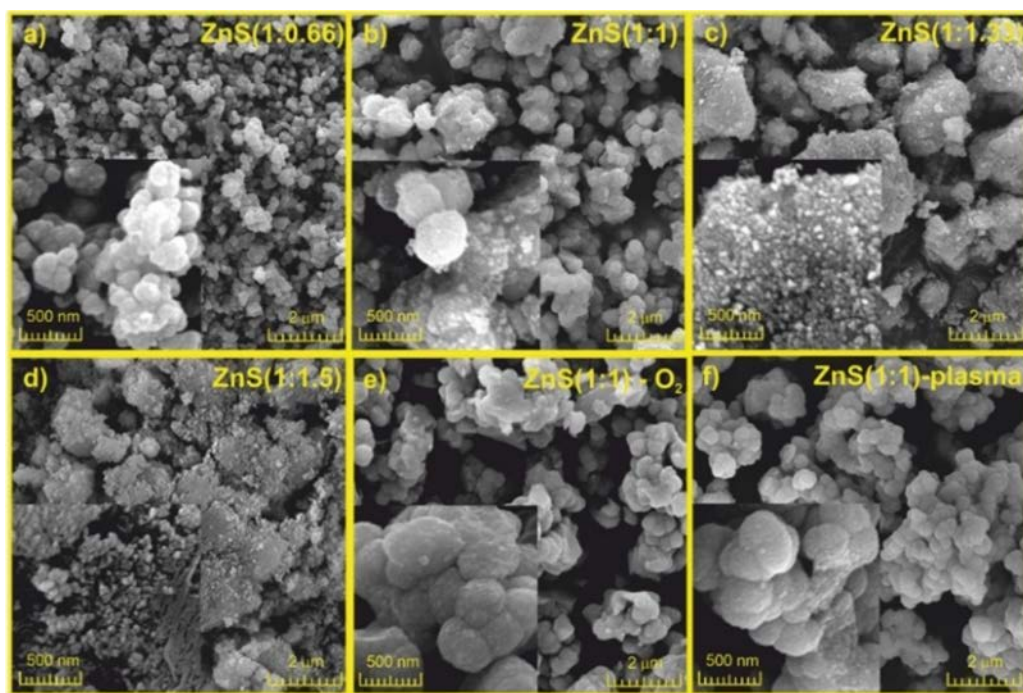
SEM images revealed that the size and shape of crystal aggregates change between ZnS(1:0.66), ZnS(1:1) (0.5−1 μm according to Figure 2a,b), ZnS(1:1.33), and ZnS(1:1.5) (1−4 μm according to Figure 2c,d). The morphology of ZnS(1:1)−O$_2$ and ZnS(1:1)−plasma materials does not differ significantly from the original ZnS(1:1) material. Based on the shape and size of the aggregates, there is no significant difference between ZnS(1:1.33) and ZnS(1:1.5). Apparently, the morphological differences are strongly influenced by the Zn:S ratio.

Elemental analysis and FAAS techniques were used to determine the final zinc and sulfur contents, respectively (Table 1). The first two samples, ZnS(1:0.66) and ZnS(1:1), appeared to be sulfur-deficient. This deficiency should be compensated with other elements, like oxygen or carbonaceous species, to keep the neutrality of the crystal lattice.

Further in-depth analysis was based on XPS. Maxima at 160.5 and 163.5 eV (Figure 3a) refer to typical sulfur 2p$_{3/2}$ and 2p$_{1/2}$ bands, respectively. Figure 3b presents Zn 2p$_{3/2}$ and 2p$_{1/2}$ bands, typical for zinc sulfide materials. There is no evidence of different species other than lattice Zn^{2+} and S^{2-}. Moreover, XPS results point out that there are only traces of carbon in the samples (Figure S4), which cannot be responsible for the different colors of the ZnS(1:1.33) and ZnS(1:1.5) samples. Finally, the signal at *ca.* 532 eV points to the presence of oxygen (O 1s; Figure 3c), the content of which can significantly vary in different materials. The positions of deconvoluted peaks (Figure 3d) for ZnS(1:1) confirm the presence of various oxygen species: surface OH groups, lattice O^{2-}, and chemisorbed oxygen molecules.[31] According to Figure 3c, the highest oxygen content has been detected in the materials with the deficiency of sulfur in the structure. This confirms that the neutrality of crystals is achieved mainly by introduced oxygen. Noticeably, ZnS(1:1) synthesized in the presence of oxygen presents an insignificant difference in the oxygen content compared to ZnS(1:1) synthesized under anaerobic conditions. It shows that the ratio between zinc and sulfur precursors has a higher influence on the final oxygen content than the synthesis conditions.

Photophysical Properties. The DRS measurements illustrate that materials with a deficiency of sulfur do not absorb visible light while materials with an excess of sulfur absorb it, as evidenced by absorption tails that span the entire range of visible light (Figure 4). Furthermore, the Tauc transformation of the Kubelka−Munk function has been used to determine the bandgap energies of the prepared materials (Table S1).[32] The bandgap energies of materials ZnS(1:0.66) and ZnS(1:1) are higher (3.53−3.60 eV) than those of ZnS(1:1.33) and ZnS(1:1.5) (3.45 eV). The decrease in the bandgap energy follows the increase in particle size (excluding ZnS(1:1)−O$_2$). The oxygen plasma treatment does not influence the light absorption properties; however, the synthesis under the oxygen atmosphere leads to the material with reduced bandgap energy (Figure 4).

The emission spectra of zinc sulfides (Figure 5) upon the excitation at 330 nm (at room temperature) show significant differences between the shapes of emission bands. Figure 5a

Figure 1. XRD patterns of synthesized zinc sulfide materials. For clarity, the JCPDS card #00-080-0020 of ZnS has been added.

Figure 2. SEM images for (a) ZnS(1:0.66), (b) ZnS(1:1), (c) ZnS(1:1.33), (d) ZnS(1:1,5), (e) ZnS(1:1)−plasma, and (f) ZnS(1:1)−O₂ materials.

Table 1. Measured Zn/S Composition of Synthesized Materials

| sample	determined composition
ZnS(1:0.66)	$ZnS_{0.87}$
ZnS(1:1)	$ZnS_{0.93}$
ZnS(1:1.33)	$ZnS_{1.00}$
ZnS(1:1.5)	$ZnS_{1.07}$

exhibits the broadening of emission spectra for materials with a deficiency of sulfur. Deconvolution of the emission bands depicted in Figure 5c,d revealed the presence of a minimum of two components in materials exhibiting an excess of sulfur, while a minimum of three components have been identified in the materials with a deficiency of sulfur. This finding highlights the complexity of the emission spectra, indicating that the observed emissions arise from multiple mechanisms operating for each material. The most intense band with a maximum of ca. 2.4 eV corresponds to the typical green emission (515 nm) of ZnS.[26] The 2.1 eV peak, the orange emission (590 nm) of ZnS reported in the literature,[33] is also observed for all tested materials. The peak centered at 2.6 eV is most likely an instrumental artifact, and therefore, no specific emission pathway can be ascribed to it. The higher energy component is particularly pronounced for sulfur-deficient materials and appears at ca. 2.8 eV (blue emission),[27] causing a broadening of the emission band. ZnS(1:1)−O₂ and ZnS(1:1)−plasma materials show quite similar emission spectra compared to ZnS(1:1) (Figure 5b). The main difference, especially at high energies, is reflected in the intensity ratios of single components.

Spectra presented in Figure 5 were recorded upon excitation with energy higher than the bandgap energy (ca. 3.5 eV of the bandgap compared to 3.8 eV of the excitation). To further extend the information on the emission properties of the materials, the 2D maps were recorded for one material with the deficiency (Figure 6a) and one with the excess (Figure 6b) of sulfur. Horizontal lines at λ_{exc} = 330 nm correspond to spectra presented in Figure 5. Noteworthily, both groups of materials show an additional strong emission signal upon irradiation in the visible-light range (360−470 nm), below the bandgap energy. Moreover, this emission for materials with a deficiency of sulfur is significantly more intense than the emission recorded upon band-to-band excitation. Since data presented in Figure 6 were normalized for the excitation light intensity (vide Experimental Section) and light absorption by materials is significantly lower at 410−420 nm than 330 nm (Figure 4), we can conclude that the quantum yield of visible-light-induced emission is drastically higher than for the band-to-band excitation. Another very interesting observation is the emission saddle at 360 nm in the case of materials with sulfur excess (Figure 6b, Figure S5), which separates visible-light induced from UV-light-induced emission. In addition, Figure S7 reveals two independent emission bands with maxima at 550 and 600 nm (excitation at 410 nm).

Furthermore, the emission decay at three wavelengths (440, 515, and 600 nm) was recorded, with band-to-band excitation (336 nm) and visible-light excitation (465 nm). Emission lifetimes were determined from the exponential decay traces (Figure 6c,d). The emission lifetimes are longer for the band-to-band excitation and increase with increasing emission wavelengths (Figure S8). In the case of visible-light excitation, lifetimes are shorter and practically independent of the emission wavelength. This behavior can be attributed to different relaxation pathways for both excitation conditions—the band-to-band excitation encompasses relaxation to deep electronic states, while visible-light excitation directly to these states reduces the relaxation pathways.

Based on the spectroscopic properties, the possible pathways of excitation and relaxation can be proposed for the studied materials. The difference between the bandgap energy (ca. 3.5 eV) and the highest energy emission (2.8 eV) leads to the
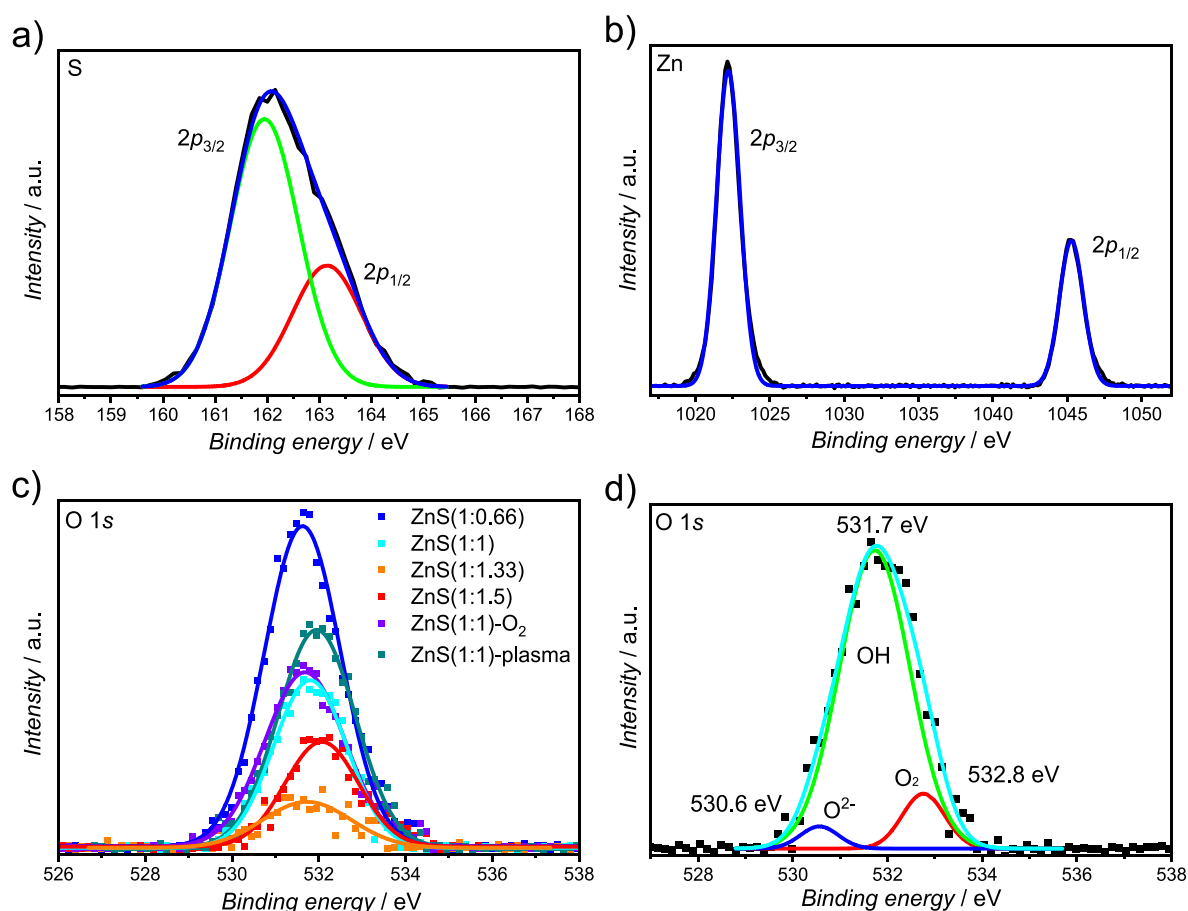
Figure 3. XPS spectra of ZnS(1:1.33) (a, b), comparison of the oxygen region for all tested samples (c), and exemplary analysis of the O 1s region for ZnS(1:1) (d).
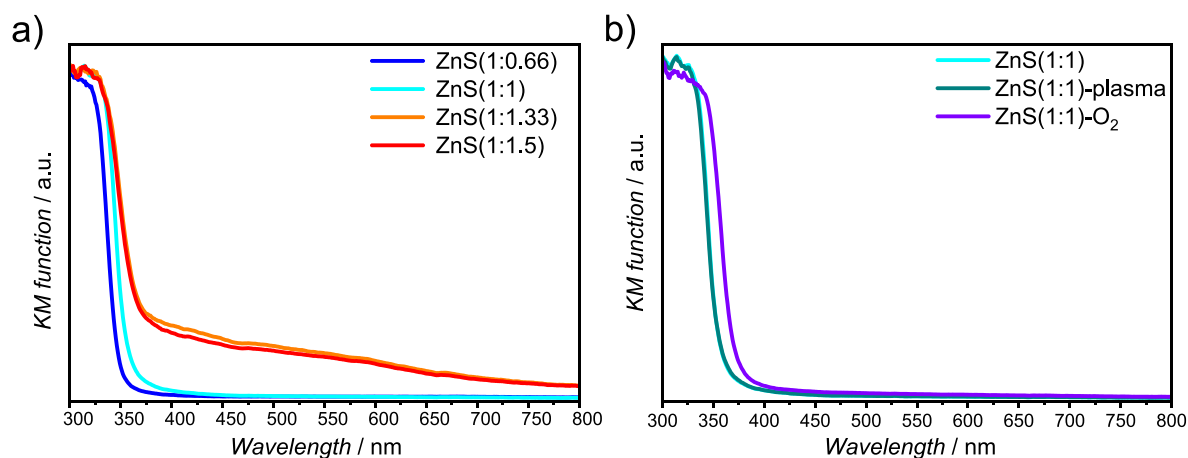

Figure 4. Kubelka−Munk spectra of (a) materials with different Zn:S ratios and (b) materials synthesized under the oxygen conditions.

conclusion that the electron loses a substantial part of its energy before reaching the state from which the emission proceeds. In other words, the deep interband states have to be present in the zinc sulfide structure. There are no discrete energy levels but rather interband states in the form of a broad band-like structure (here denoted as region I; Figure 7). Such arrangements are confirmed by the excitation−emission maps (Figure S7, especially excitation spectra, Figure S6), where all observed emissions originate from a broad excitation region (ranging from 3.3 to 2.6 eV, Figure 6). For sulfur-rich

materials, region I does not reach the conduction band edge. Region I is therefore separated from the conduction band with region II (*ca.* 3.3−3.5 eV above VB; Figure 7), characterized by a low emission intensity. Noteworthily, this low intensity of emission is not substantiated by the absorption spectra (*vide* Figure 4). Therefore, it can be concluded that the excitation to these states (region II) favors non-radiative relaxations (Figure 7).

The excitation to region I is associated with two emission bands (2.1 and 2.4 eV), which disappear below the same
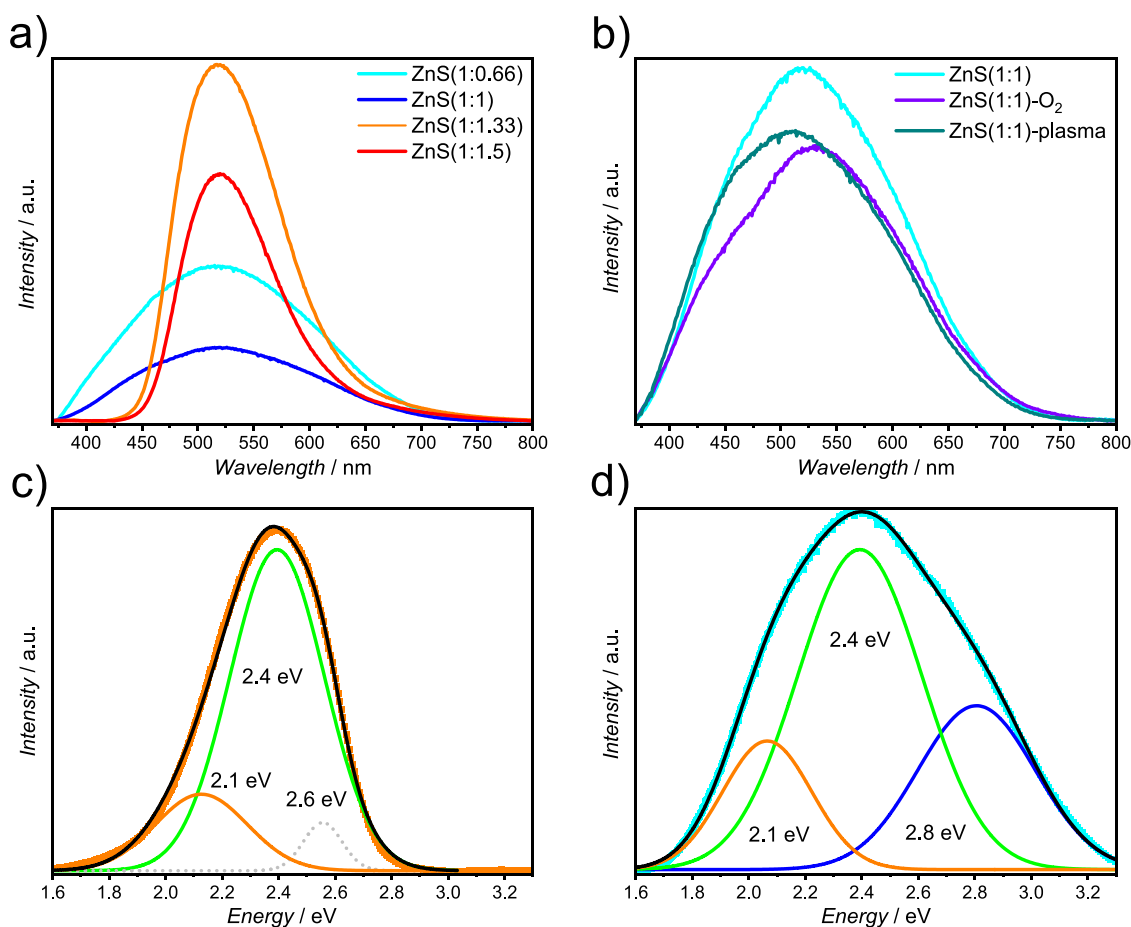
Figure 5. Emission spectra of the studied materials (a, b); deconvolution of spectra of ZnS(1:1.33) (c) and ZnS(1:1) (d). The excitation wavelength is 330 nm. Spectra collected with the use of a 370 nm cutoff filter.

excitation energy. This behavior confirms that both signals have the same origin, most likely the low energy edge of region I (according to Kasha's rule). Furthermore, the energy difference between the bottom edge of region I and the top of the valence band is higher than the energy of respective emissions (2.6 vs 2.4 and 2.1 eV, respectively). Therefore, at least two groups of electronic states must exist, 0.2 and 0.5 eV above the valence band (Figure 7). For the sulfur-deficient materials, an additional blue emission was observed (2.8 eV). We hypothesize that such emission is associated with the abovementioned states. However, both pathways differ in kinetics, as confirmed by the emission decay measurements (Figure S8). Therefore, other electronic states must exist below the conduction band edge, from which this emission originates. It means there is a range of energy of states offering two possible pathways of electron relaxation (resulting in green/ orange or blue emissions). However, both pathways differ in kinetics, as confirmed by the emission decay measurements (Figure S8).

Spectroelectrochemical Determination of Electronic States. The proposed model of the electronic structure of zinc sulfides constructed based on spectroscopic properties (Figure 7) contains electronic states, the energy of which is related to the bands' positions. Such an approach cannot place the discussed structure in the absolute energy scale; however, learning the energy of any level from Figure 7 gives the possibility to solve this problem. The most obvious parameter would be the conduction band edge potential. However, in the

literature, this value varies in the range from -1.8 to -0.8 V vs SHE;[15,34−40] therefore, this value cannot be used for calibration of the energy. Recently, we proposed the modification of a spectroelectrochemical (SE-DRS) method that allows determining the energy and density of electronic states below the bottom of the conduction band.[41] The SE-DRS method, unfortunately, does not give the possibility to unambiguously determine the position of the bottom of the conduction band without combining it with other techniques.[42] Since this method allows observing the electronic states, the positions of which are also determined by the discussed spectroscopic approach, there is a possibility to use it for the calibration of our model. Figure 8 shows the relative density of electronic states (DOS) for the tested zinc sulfides. The shape of the DOS curve changes between materials, but the electronic density onset appears around the same potential $(-0.8$ V vs SHE). A slight shift is observed for the ZnS(1:1)− O_2 material, for which the onset potential is -0.9 vs SHE. The DOS of materials with different zinc-to-sulfur ratios have similar patterns. Two groups of states can be distinguished: low energy (from -0.8 to -1.1 V vs SHE) and high energy (from -1.1 to -1.4 V vs SHE) states; however, there is an exception for ZnS(1:1)−O_2. The electronic states of all materials are within potential ranges that seem to be too positive for the zinc sulfide conduction band. At the same time, they are quite wide, in accordance with spectroscopically postulated inter-band states.
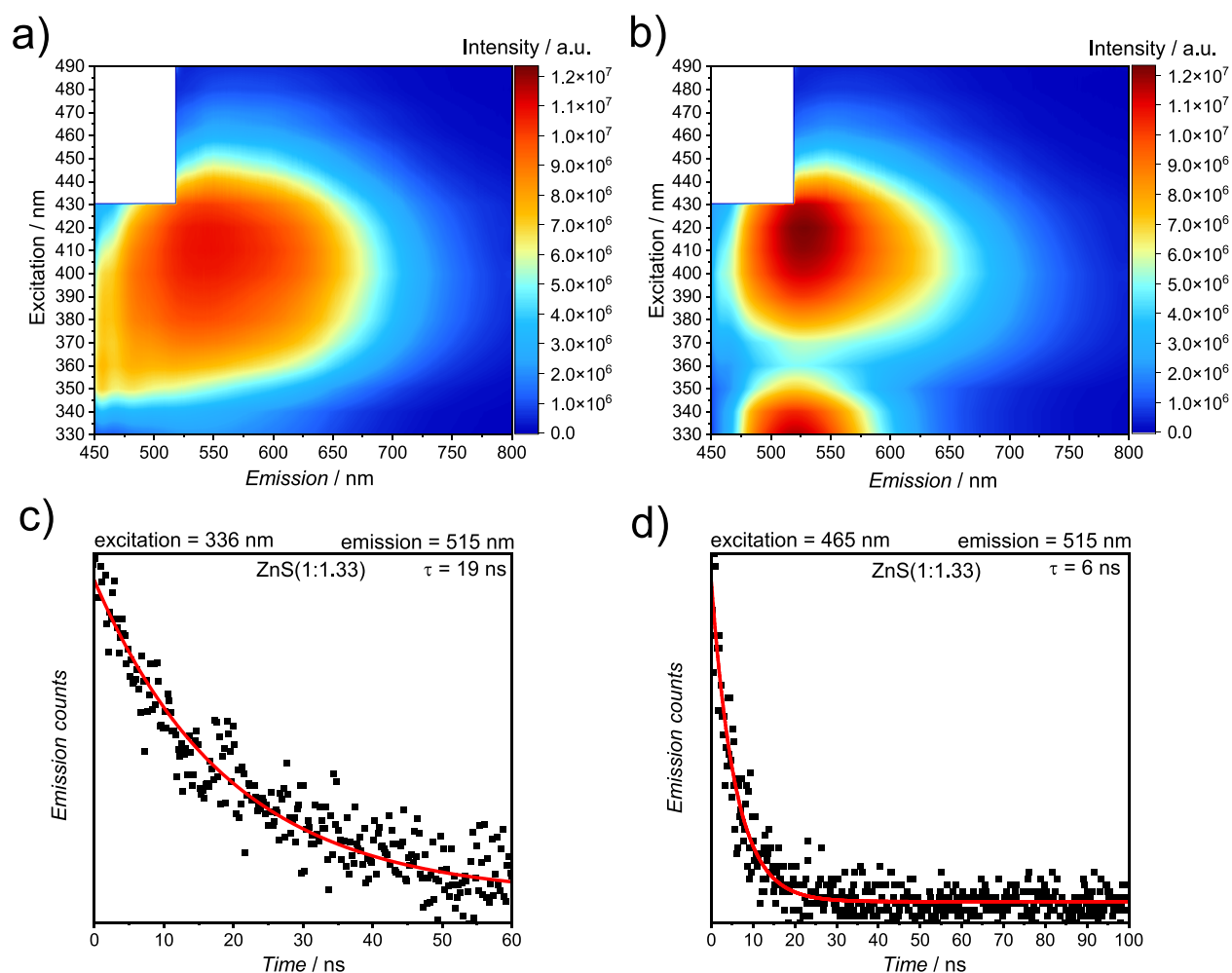
Figure 6. 2D maps of emission intensity in the function of both excitation and emission wavelengths. Figures present the emission spectra of ZnS(1:1) (a) and ZnS(1:1.33) (b). Emission decays for ZnS(1:1.33) were recorded at 515 nm upon excitation at 336 nm (c) and 465 nm (d).

Noteworthily, DOS for both samples of ZnS(1:1) synthesized under different conditions (ZnS(1:1)−O_2, ZnS(1:1)−plasma) vary from the original sample. In the case of ZnS(1:1)−O_2, it is not surprising since this sample differs in many ways from ZnS(1:1). Much more striking is the lack of DOS similarity for ZnS(1:1)−plasma and ZnS(1:1) samples. Treating the ZnS(1:1) sample with oxygen plasma was supposed to induce changes in surface defects. Up to now, most measurements have shown no differences from the original ZnS(1:1), except for the emission spectra and the DOS profiles. The spectroelectrochemical method seems to be particularly sensitive to such potentially insignificant changes, as already demonstrated elsewhere.[43] The fact that emission and DOS vary when only the surface is modified points to the same origin of these changes, *i.e.*, to surface states. Moreover, this observation strengthens our hypothesis for using the onset potential of DOS to position our model at the potential scale.

The DOS profiles were overlain with the spectroscopic potentials of the bands' edges. The obtained values are −1.7 V *vs* SHE for CB and +1.8 V *vs* SHE for VB. These values are in the lower limits of the reported potentials.[34,39] Moreover, it is possible to estimate the potential values of two groups of states localized above the valence band edge, at 1.3 and 1.6 V *vs* SHE, respectively. The energy of electrons, excited to both CB and electron traps, is apparently not sufficient to reduce CO_2 to $CO_2^{\bullet-}$ radical (reported to be −1.9 V *vs* SHE[44,45]) but should

still facilitate its multielectron reduction, as well as hydrogen evolution. Previously, we have reported $CO_2^{\bullet-}$ radical formation at irradiated ZnS (confirmed by EPR spectroscopy);[46] therefore, we postulate that this one-electron reaction should be possible also under milder conditions (potentials higher than −1.9 V). To the best of the authors' knowledge, no such hypothesis has been postulated for ZnS so far. Interestingly, mechanisms of CO_2 reduction by various photocatalysts, which are assumed to proceed through a one-electron reduction of activated $CO_{2(ads)}$ to $CO_2^{\bullet-}{}_{(ads)}$, have been reported several times. Most photocatalysts, including TiO_2, upon excitation cannot offer potentials as low as −1.9 V. It should be stressed that the adsorbed and therefore activated CO_2 molecule, due to the loss of its linearity, should be prone to reduction at milder potentials. This explains the apparent contradiction between the redox properties of ZnS and the requirements for one-electron CO_2 reduction.

Photoactivity. Photocurrent measurements in the function of incident light wavelength are presented in Figure 9. More detailed results, showing photocurrent measurements as the function of both wavelength and electrode potential, are included in the SI (Figure S9). The onsets of photocurrents are at *ca.* 480 nm for ZnS(1:1.33) and ZnS(1:1.5) and *ca.* 460 nm for ZnS(1:0.66) and ZnS(1:1). It is noteworthy that not only ZnS(1:1.33) and ZnS(1:1.5), which have intense absorption tail in the visible range (see Figure 4), but also ZnS(1:0.66)
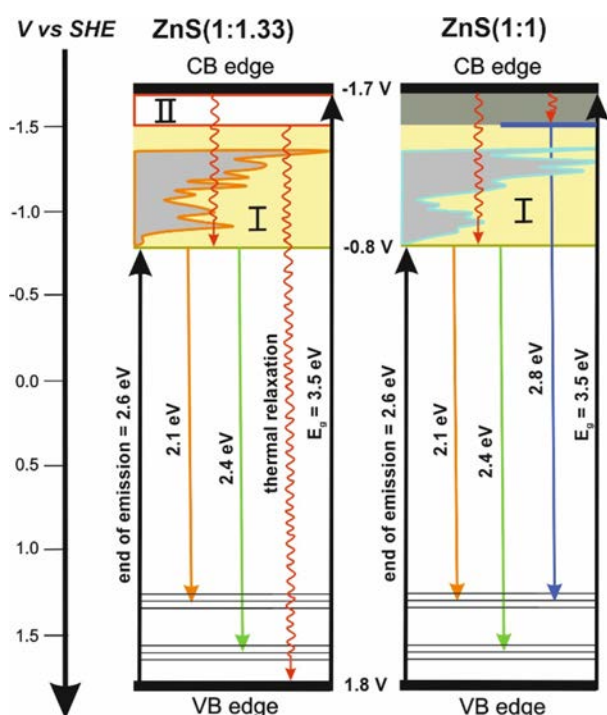
Figure 7. Proposed electronic structure constructed for the studied materials.

and ZnS(1:1) can generate photocurrents in the visible light range. The variation in photocurrent generation efficiency in the visible-light range reflects rather the overall photo-electrochemical activity than the difference in the light absorption in this range. It implies that the excitation within the interband states may cause the generation of charge carriers. Moreover, the wavelength onset for which photo-currents are generated is in good agreement with the prediction based on the proposed model (Figure 7). The

high photoelectrochemical activity was observed for materials with an excess of sulfur, with the highest photocurrents for ZnS(1:1.33) (Figure 9a). These observations further confirm the influence of the Zn:S ratio on the efficiency of charge generation, separation, and recombination and point to the highest efficiency separation, recombination, and point to the highest efficiency of the interfacial electron transfer (IFET) for ZnS(1:1.33). Noteworthily, IFET has been only slightly influenced by the oxygen plasma treatment (Figure 9b), despite the noticeable impact of this modification on the surface states discussed above. ZnS(1:1)−O$_2$, as a material significantly different from those synthesized under anaerobic conditions, presents a miserable photoelectrochemical activity (Figure S10).

The photocatalytic activity of ZnS samples has been tested in dehydrodimerization of 2,5-dihydrofuran reaction, with simultaneous hydrogen evolution, under UV-light illumination (Figure 10a). The reaction progress is linear, pointing to the pseudo-zero-order kinetics. Again, the materials with an excess of sulfur are more active. The plasma surface treatment diminished photocatalytic hydrogen generation, in accordance with the efficiency of the IFET process discussed above (Figure S10). ZnS(1:1)−O$_2$ shows almost six times lower photocatalytic activity compared to ZnS(1:1). Therefore, these materials were excluded from further photocatalytic tests. In addition to hydrogen generation, also carbon dioxide reduction was tested. In this experiment, CO$_2$ was provided in the form of the sodium bicarbonate solution (pH = 8.3). Only formate was observed as a product in the liquid phase (Figure 10b), while no products (*e.g.*, hydrogen or carbon monoxide) were detected in the gas phase. Furthermore, materials with an excess of sulfur revealed their higher activity compared to materials with a deficiency of sulfur. The formate generation did not correlate with the Zn:S ratio; there are rather two groups of activities, in accordance with the discussed two
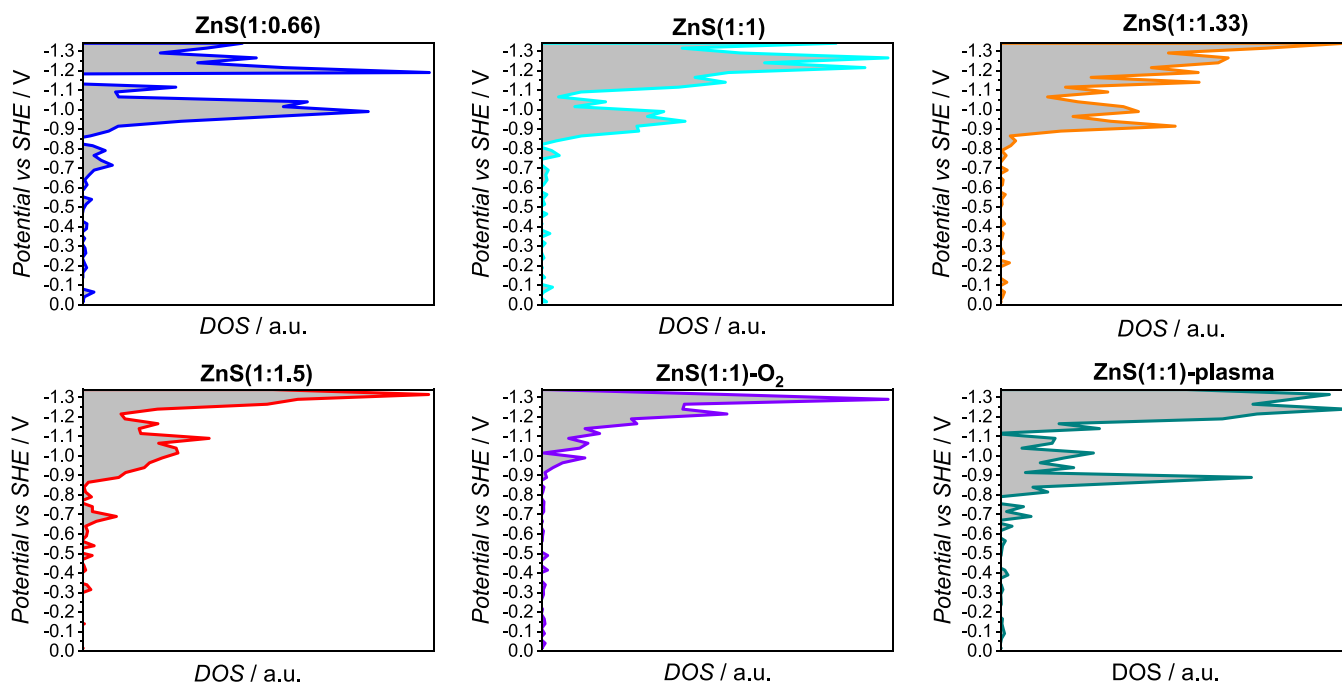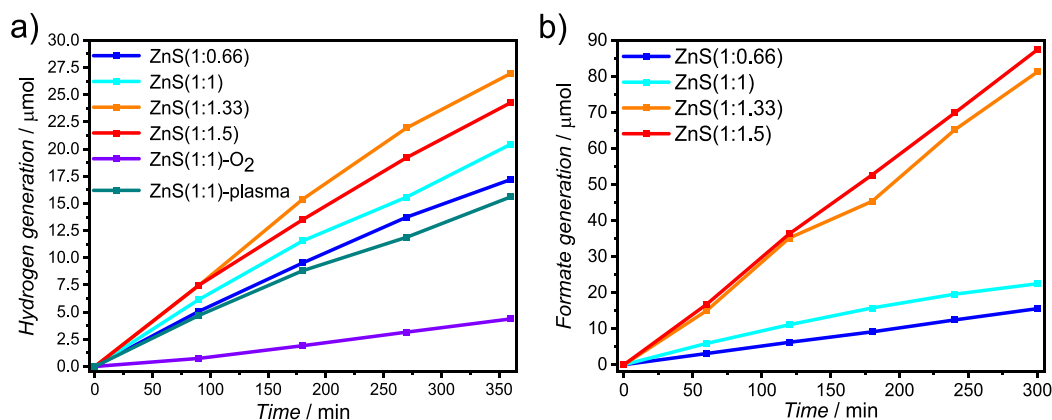

Figure 8. Results of spectroelectrochemical measurements. Plots include the arbitral values of the DOS in the function of applied voltage.
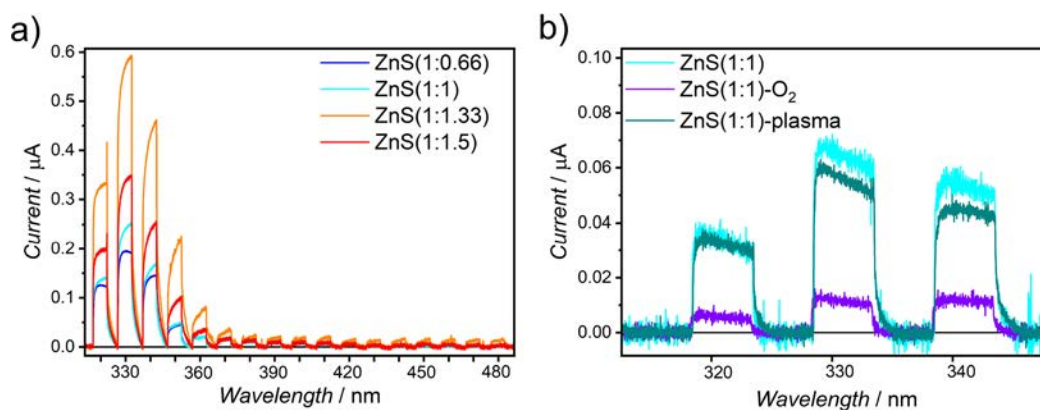
Figure 9. Photocurrent *vs* wavelength at 1 V *vs* Ag/AgCl recorded for materials with different Zn:S ratios (a) and ZnS(1:1) unmodified and modified with oxygen plasma (b).

Figure 10. Hydrogen generation in the presence of 2,5-dihydrofuran (a) and CO_2 reduction to formate (b).

groups of materials, sulfur-deficient and sulfur-rich, classified according to the presented schemes (Figure 7).

Photocurrent, hydrogen, and formate generation efficiencies for ZnS(1:0.66), ZnS(1:1), ZnS(1:1.33), and ZnS(1:1.5) were compared in Figure 11. There is a correlation between photocatalytic and photoelectrochemical activity. Therefore, the rates of both water and carbon dioxide reduction reactions are primarily governed by IFET processes. In addition, the adsorption efficiency of 2,5-dihydrofuran is compared to the hydrogen production rate (Figure S11). The dominant role of specific surface area in hydrogen generation was excluded.
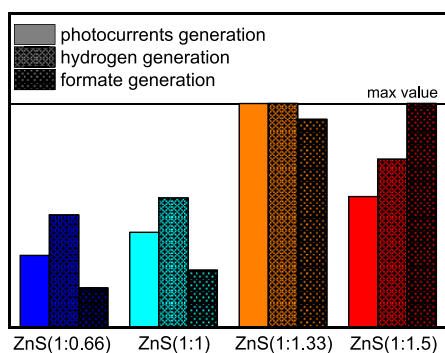
Figure 11. The comparison of photocurrents, hydrogen, and formate generation efficiency at materials with a different Zn:S ratio. The photocurrents or reaction rates were normalized to the highest value in the series.

■ CONCLUSIONS

Materials with a different Zn:S ratio were synthesized and characterized. The powders can be divided into two groups (sulfur-deficient and sulfur-rich) by their morphology, photophysical properties, and photoactivity. In addition, the influence of oxygen used during ZnS precipitation and post-synthetically (plasma treatment) was tested for ZnS(1:1). Despite the lack of morphological changes, ZnS(1:1)−plasma exhibited different electronic properties and, therefore, different photoactivities. ZnS(1:1)−O_2 differs significantly in both physicochemical properties and diminished photoactivity. Interestingly, the customization of the Zn:S ratio more strongly influences the final concentration of oxygen in the ZnS structure (the highest concentration for ZnS(1:0.66)), than the use of the oxygen-rich reactor atmosphere. Therefore, a synthesis of ZnS photocatalysts under an oxygen-free atmosphere appears to be more favorable.

The photoluminescence measurements elucidated a difference in the electronic properties of sulfur-rich and sulfur-deficient materials. Both groups of zinc sulfide exhibit green (*ca.* 515 nm) and orange (*ca.* 590 nm) emission lines. An additional emission component has been observed for sulfur-deficient materials (blue emission at *ca.* 440 nm), which may be related to the lower photocatalytic activity. The ZnS energy schemes presented in Figure 7 were constructed based on the energy of particular emission components. Furthermore, spectroelectrochemical measurements revealed the differences in the distribution of interband states (Figure 8). The combination of all applied techniques enabled the recognition

of the energy of interband states and CB, as well as their role in photoinduced processes. Moreover, the energy of electronic states above the valence band edge was estimated. Our model shows that despite the strongly negative position of the CB edge (-1.7 V vs SHE), the effective reduction potential of photogenerated electrons should be associated with interband states at $ca.$ -0.8 V vs SHE, $i.e.$, at almost 1 V more positive values. This difference can appear to be a "game-changer"; therefore, it should be taken into account in a rational designing of an active photocatalyst. In this context, $CO_2^{\bullet-}$ generation reported previously for these materials should proceed under significantly milder conditions than the commonly reported potential of -1.9 V vs SHE. This can be rationalized by the activation of carbon dioxide upon adsorption. With electrons trapped at -0.8 V vs SHE, the tested materials still enable the reduction of carbon dioxide and water to formic acid and hydrogen, respectively, as demonstrated in photocatalytic tests. The presented analysis shows a very useful approach to the detailed characterization of effective redox properties of excited semiconductors.

■ ASSOCIATED CONTENT

Ⓢ Supporting Information

The Supporting Information is available free of charge at https://pubs.acs.org/doi/10.1021/acs.jpcc.3c04298.

> Tauc plots; crystallite size and bandgap energies; XPS spectra; excitation spectra; emission maps; emission decays; photocurrent maps; and additional photo-catalytic activity comparison (PDF)

■ AUTHOR INFORMATION

Corresponding Authors

Marcin Kobielusz − *Faculty of Chemistry, Jagiellonian University, Kraków 30-387, Poland;* ⓞ orcid.org/0000-0003-2707-0415; Email: kobielusz@chemia.uj.edu.pl

Wojciech Macyk − *Faculty of Chemistry, Jagiellonian University, Kraków 30-387, Poland;* ⓞ orcid.org/0000-0002-1317-6115; Email: macyk@chemia.uj.edu.pl

Authors

Krystian Mróz − *Faculty of Chemistry, Jagiellonian University, Kraków 30-387, Poland; Doctoral School of Exact and Natural Sciences, Jagiellonian University, Kraków 30-348, Poland*

Łukasz Orzeł − *Faculty of Chemistry, Jagiellonian University, Kraków 30-387, Poland*

Complete contact information is available at:
https://pubs.acs.org/10.1021/acs.jpcc.3c04298

Author Contributions

The manuscript was written through contributions of all authors.

Notes

The authors declare no competing financial interest.

■ ACKNOWLEDGMENTS

■ ABBREVIATIONS

SE-DRS, diffuse reflectance spectroelectrochemistry; CB, conduction band; RDB-PAS, reverse double-beam photo-acoustic spectroscopy; PL, photoluminescence; XPS, X-ray photoelectron spectroscopy; TBAP, tetrabutylammonium perchlorate; XRD, X-ray diffraction; SEM, scanning electron microscopy; KM, Kubelka−Munk function; λ_{exc}, excitation wavelength; VB, valence band; SHE, standard hydrogen electrode; IFET, interfacial electron transfer; SI, supporting information

■ REFERENCES

(1) Meng, Y.; Liu, G.; Zuo, G.; Meng, X.; Wang, T.; Ye, J. A review on ZnS-based photocatalysts for CO_2 reduction in all-inorganic aqueous medium. *Nanoscale* **2022**, *14*, 14455−14465.

(2) Kanemoto, M.; Hosokawa, H.; Wada, Y.; Murakoshi, K.; Yanagida, S.; Sakata, T.; Mori, H.; Ishikawa, M.; Kobayashi, H. Semiconductor photocatalysis. Part 20.-Role of surface in the photoreduction of carbon dioxide catalysed by colloidal ZnS nanocrystallites in organic flush. *J. Chem. Soc., Faraday Trans.* **1996**, *92*, 2401−2411.

(3) Jing, C.; Ying-Feng, L.; Weng-Bin, S.; Jia-Dong, H.; Zhong-Yan, M. Photocatalytic Reduction of CO_2 by Nano-Sized ZnS Supported on Silica and Polyvinyl Alcohol. *J. Shanghai Univ. (Engl. Ed.)* **2003**, *7*, 289−293.

(4) Tsuji, I.; Kato, H.; Kobayashi, H.; Kudo, A. Photocatalytic H_2 Evolution under Visible-Light Irradiation over Band-Structure-Controlled $(CuIn)_xZn_{2(1-x)}S_2$ Solid Solutions. *J. Phys. Chem. B* **2005**, *109*, 7323−7329.

(5) Kudo, A.; Sekizawa, M. Photocatalytic H_2 evolution under visible light irradiation on Ni-doped ZnS photocatalyst. *Chem. Commun.* **2000**, *36*, 1371−1372.

(6) Reber, J.; Meier, K. Photochemical Production of Hydrogen with Zinc Sulfide Suspensions. *J. Phys. Chem.* **1984**, *88*, 5903−5913.

(7) Aubert, T.; Golovatenko, A. A.; Rodina, A. V.; Hens, Z. Comment on "Size Dependent Optical Properties and Structure of ZnS Nanocrystals Prepared from a Library of Thioureas". *Chem. Mater.* **2022**, *34*, 6182−6184.

(8) Bennett, E.; Greenberg, M. W.; Jordan, A. J.; Hamachi, L. S.; Banerjee, S.; Billinge, S. J. L.; Owen, J. S. Size Dependent Optical Properties and Structure of ZnS Nanocrystals Prepared from a Library of Thioureas. *Chem. Mater.* **2022**, *34*, 706−717.

(9) Yu, D.; Fang, H.; Qiu, P.; Meng, F.; Liu, H.; Wang, S.; Lv, P.; Cong, X.; Niu, Q.; Li, T. Improving the performance of ZnS photocatalyst in degrading organic pollutants by constructing composites with Ag_2O. *Nanomaterials* **2021**, *11*, 1451.

(10) Wang, W.; Lee, G.-J.; Wang, P.; Qiao, Z.; Liu, N.; Wu, J. J. Microwave synthesis of metal-doped ZnS photocatalysts and applications on degrading 4-chlorophenol using heterogeneous photocatalytic ozonation process. *Sep. Purif. Technol.* **2020**, *237*, No. 116469.

(11) Kanakaraju, D.; Chandrasekaran, A. Recent advances in TiO_2/ZnS-based binary and ternary photocatalysts for the degradation of organic pollutants. *Sci. Total Environ.* **2023**, *868*, No. 161525.

(12) Murillo-Sierra, J. C.; Hernández-Ramírez, A.; Pino-Sandoval, D. A.; Ruiz-Ruiz, E.; Martínez-Hernández, A. Promoting multielectron CO_2 reduction using a direct Z-scheme WO_3/ZnS photocatalyst. *J. CO2 Util.* **2022**, *63*, No. 102122.

(13) Sabbah, A.; Shown, I.; Qorbani, M.; Fu, F.-Y.; Lin, T.-Y.; Wu, H.-L.; Chung, P.-W.; Wu, C.-I.; Santiago, S. R. M.; Shen, J.-L.; Chen, K. H.; Chen, L. C. Boosting photocatalytic CO_2 reduction in a ZnS/$ZnIn2S_4$ heterostructure through strain-induced direct Z-scheme and a mechanistic study of molecular CO_2 interaction thereon. *Nano Energy* **2022**, *93*, No. 106809.

(14) Zhang, X.; Kim, D.; Lee, L. Y. S. Copper-doped ZnS with internal phase junctions for highly selective CO production from CO_2 photoreduction. *ACS Appl. Energy Mater.* **2021**, *4*, 2586−2592.

(15) Hao, X.; Wang, Y.; Zhou, J.; Cui, Z.; Wang, Y.; Zou, Z. Zinc vacancy-promoted photocatalytic activity and photostability of ZnS for efficient visible-light-driven hydrogen evolution. *Appl. Catal. B* **2018**, *221*, 302−311.

(16) Khan, S.; Je, M.; Ton, N. N. T.; Lei, W.; Taniike, T.; Yanagida, S.; Ogawa, D.; Suzuki, N.; Terashima, C.; Fujishima, A.; Choi, H.; Katsumata, K. I. C-doped ZnS-ZnO/Rh nanosheets as multi-junctioned photocatalysts for effective H$_2$ generation from pure water under solar simulating light. *Appl. Catal. B* **2021**, *297*, No. 120473.

(17) Yuan, L.; Qi, M. Y.; Tang, Z. R.; Xu, Y. J. Coupling strategy for CO$_2$ valorization integrated with organic synthesis by heterogeneous photocatalysis. *Am. Ethnol.* **2021**, *133*, 21320−21342.

(18) Hosseini-Sarvari, M.; Sheikh, H. Reduced graphene oxide−zinc sulfide (RGO−ZnS) nanocomposite: a new photocatalyst for oxidative cyclization of benzylamines to benzazoles under visible-light irradiation. *React. Chem. Eng.* **2022**, *7*, 2202−2210.

(19) Kisch, H., *Semiconductor photocatalysis: principles and applications*. John Wiley & Sons, 2014.

(20) Chakraborty, I. N.; Roy, S.; Devatha, G.; Rao, A.; Pillai, P. P. InP/ZnS quantum dots as efficient visible-light photocatalysts for redox and carbon−carbon coupling reactions. *Chem. Mater.* **2019**, *31*, 2258−2262.

(21) Tahir, M.; Tasleem, S.; Tahir, B. Recent development in band engineering of binary semiconductor materials for solar driven photocatalytic hydrogen production. *Int. J. Hydrogen Energy* **2020**, *45*, 15985−16038.

(22) Saleh, M.; Lynn, K. G.; Jacobsohn, L. G.; McCloy, J. S. Luminescence of undoped commercial ZnS crystals: A critical review and new evidence on the role of impurities using photoluminescence and electrical transient spectroscopy. *J. Appl. Phys.* **2019**, *125*, No. 075702.

(23) Lahariya, V.; Dhoble, S. J. Development and advancement of undoped and doped zinc sulfide for phosphor application. *Displays* **2022**, *74*, No. 102186.

(24) Dai, L.; Strelow, C.; Kipp, T.; Mews, A.; Benkenstein, I.; Eifler, D.; Vuong, T. H.; Rabeah, J.; McGettrick, J.; Lesyuk, R. Colloidal manganese-doped ZnS Nanoplatelets and their optical properties. *Chem. Mater.* **2020**, *33*, 275−284.

(25) Ho, Q.; Castillo, M. Defects study in zinc blende ZnS utilizing optimized hybrid functional. *Comput. Mater. Sci.* **2023**, *216*, No. 111827.

(26) Zhang, Y.-P.; Liu, W.; Liu, B.-D.; Wang, R.-M. Morphology−structure diversity of ZnS nanostructures and their optical properties. *Rare Met.* **2014**, *33*, 1−15.

(27) Fang, X.; Bando, Y.; Gautam, U. K.; Zhai, T.; Zeng, H.; Xu, X.; Liao, M.; Golberg, D. ZnO and ZnS Nanostructures: Ultraviolet-Light Emitters, Lasers, and Sensors. *Crit. Rev. Solid State Mater. Sci.* **2009**, *34*, 190−223.

(28) Becker; Bard, A. J. Photoluminescence and photoinduced oxygen adsorption of colloidal zinc sulfide dispersions. *J. Phys. Chem.* **1983**, *87*, 4888−4893.

(29) Hao, E.; Sun, Y.; Yang, B.; Zhang, X.; Liu, J.; Shen, J. Synthesis and photophysical properties of ZnS colloidal particles doped with silver. *J. Colloid Interface Sci.* **1998**, *204*, 369−373.

(30) Hörner, G.; Johne, P.; Künneth, R.; Twardzik, G.; Roth, H.; Clark, T.; Kisch, H. Semiconductor Type A Photocatalysis: Role of Substrate Adsorption and the Nature of Photoreactive Surface Sites in Zinc Sulfide Catalyzed C-C Coupling Reactions. *Eur. J. Chem.* **1999**, *5*, 208−217.

(31) Poliukhova, V.; Khan, S.; Qiaohong, Z.; Zhang, J.; Kim, D.; Kim, S.; Cho, S.-H. ZnS/ZnO nanosheets obtained by thermal treatment of ZnS/ethylenediamine as a Z-scheme photocatalyst for H$_2$ generation and Cr(VI) reduction. *Appl. Surf. Sci.* **2022**, *575*, No. 151773.

(32) Makuła, P.; Pacia, M.; Macyk, W. How To Correctly Determine the Band Gap Energy of Modified Semiconductor Photocatalysts Based on UV−Vis Spectra. *J. Phys. Chem. Lett.* **2018**, *9*, 6814−6817.

(33) Wang, X.; Shi, J.; Feng, Z.; Li, M.; Li, C. Visible emission characteristics from different defects of ZnS nanocrystals. *Phys. Chem. Chem. Phys.* **2011**, *13*, 4715−4723.

(34) Wojtyła, S.; Baran, T. Photocatalytic H$_2$ production over RuO$_2$@ZnS and RuO$_2$@CuS nanostructures. *Int. J. Hydrogen Energy* **2019**, *44*, 14624−14634.

(35) Ye, Z.; Kong, L.; Chen, F.; Chen, Z.; Lin, Y.; Liu, C. A comparative study of photocatalytic activity of ZnS photocatalyst for degradation of various dyes. *Optik* **2018**, *164*, 345−354.

(36) Maarisetty, D.; Mahanta, S.; Sahoo, A. K.; Mohapatra, P.; Baral, S. S. Steering the Charge Kinetics in Dual-Functional Photocatalysis by Surface Dipole Moments and Band Edge Modulation: A Defect Study in TiO$_2$-ZnS-rGO Composites. *ACS Appl. Mater. Interfaces* **2020**, *12*, 11679−11692.

(37) Talukdar, S.; Dutta, R. K. A mechanistic approach for superoxide radicals and singlet oxygen mediated enhanced photo-catalytic dye degradation by selenium doped ZnS nanoparticles. *RSC Adv.* **2016**, *6*, 928−936.

(38) Hao, X.; Zhou, J.; Cui, Z.; Wang, Y.; Wang, Y.; Zou, Z. Zn-vacancy mediated electron-hole separation in ZnS/g-C$_3$N$_4$ hetero-junction for efficient visible-light photocatalytic hydrogen production. *Appl. Catal. B* **2018**, *229*, 41−51.

(39) Fan, F.-R. F.; Leempoel, P.; Bard, A. J. Semiconductor Electrodes: LI . Efficient Electroluminescence at Electrode in Aqueous Electrolytes. *J. Electrochem. Soc.* **1983**, *130*, 1866−1875.

(40) Zhou, Y.; Chen, G.; Yu, Y.; Feng, Y.; Zheng, Y.; He, F.; Han, Z. An efficient method to enhance the stability of sulphide semi-conductor photocatalysts: a case study of N-doped ZnS. *Phys. Chem. Chem. Phys.* **2015**, *17*, 1870−1876.

(41) Kobielusz, M.; Pilarczyk, K.; Świętek, E.; Szaciłowski, K.; Macyk, W. Spectroelectrochemical analysis of TiO$_2$ electronic states—implications for the photocatalytic activity of anatase and rutile. *Catal. Today* **2018**, *309*, 35−42.

(42) Kobielusz, M.; Nitta, A.; Macyk, W.; Ohtani, B. Combined Spectroscopic Methods of Determination of Density of Electronic States: Comparative Analysis of Diffuse Reflectance Spectroelectrochemistry and Reversed Double-Beam Photoacoustic Spectroscopy. *J. Phys. Chem. Lett.* **2021**, *12*, 3019−3025.

(43) Trochowski, M.; Kobielusz, M.; Mróz, K.; Surówka, M.; Hämäläinen, J.; Iivonen, T.; Leskelä, M.; Macyk, W. How insignificant modifications of photocatalysts can significantly change their photocatalytic activity. *J. Mater. Chem. A* **2019**, *7*, 25142−25154.

(44) Barrocas, B. T.; Ambrožová, N.; Kočí, K. Photocatalytic reduction of carbon dioxide on TiO$_2$ heterojunction photocatalysts—a review. *Materials* **2022**, *15*, 967.

(45) Dibenedetto, A.; Zhang, J.; Trochowski, M.; Angelini, A.; Macyk, W.; Aresta, M. Photocatalytic carboxylation of CH bonds promoted by popped graphene oxide (PGO) either bare or loaded with CuO. *J. CO2 Util.* **2017**, *20*, 97−104.

(46) Baran, T.; Dibenedetto, A.; Aresta, M.; Kruczała, K.; Macyk, W. Photocatalytic carboxylation of organic substrates with carbon dioxide at zinc sulfide with deposited ruthenium nanoparticles. *ChemPlusChem* **2014**, *79*, 708−715.